Journal of
Manufacturing and Materials Processing

MDPI

Article

A Predictive Crater-Overlap Model for EDM Finishing Relevant to AISI 304 Welded Joints

Mohsen Forouzanmehr [1,2], Mohammad Reza Dashtbayazi [1] and Mahmoud Chizari [3,*]

[1] Department of Mechanical Engineering, Shahid Bahonar University of Kerman, Kerman 76169-14111, Iran
[2] Research and Development, Copper and Copper Alloys, Shahid Bahonar Copper Industries (CSP) Co., Baghin Road, Kerman 76171-97114, Iran
[3] School of Physics Engineering and Computer Science, University of Hertfordshire, Hatfield AL10 9AB, UK
* Correspondence: m.chizari@herts.ac.uk

Abstract

Electrical Discharge Machining (EDM) enables precision post-weld finishing of AISI 304 stainless steel, but stochastic spark overlaps make the fatigue-critical maximum peak-to-valley height (R_{max}) difficult to predict. This study develops a validated physics-based framework quantifying how crater overlap governs R_{max} evolution. Experiments on unwelded AISI 304 cylinders—proxying weld metal while excluding heat-affected zone (HAZ) effects—used Central Composite Design (20 trials, 900–9380 µJ discharge energies). Profilometry and scanning electron microscopy (SEM) correlated the crater size, overlap intensity, micro-cracking, and R_{max} escalation from 18 to 85 µm. Primary and secondary crater formation under minimum and maximum overlap configurations were simulated using a 2D axisymmetric finite element model with Gaussian heat flux and temperature-dependent thermophysical properties. The predictive metric $R_{max,num} = (d_{initial} + d_{secondary})/2$ achieved 11–19% average error against the experimental $R_{max,exp}$, with complementary valley depth (R_v) validation at 13% error. The Specimen 7 outlier (~50% error) reveals the limitations of deterministic modelling under stochastic debris accumulation and plasma instability at intermediate energies. Crater overlap generates secondary dimples, sharp inter-crater peaks, and rim micro-crack networks, driving the 4.7-fold R_{max} increase—approaching International Institute of Welding (IIW) fatigue thresholds (<25 µm for high-cycle categories). The framework explicitly links the discharge energy, plasma channel radius (R_{pc}), and overlap geometry to surface topography, enabling process optimization ($I \cdot t_{on} < 60$ A·s maintains $R_{max} < 25$ µm). Mesh independence (<2.5% convergence) and six centre-point replicates (CV = 4.2%) confirm robustness. This validated upper-bound R_{max} predictor supports the digital co-optimization of welding and EDM parameters for aerospace/energy applications, with planned extensions to stochastic 3D models incorporating adaptive remeshing and real weld topographies.

Keywords: electrical discharge machining (EDM); surface integrity; maximum peak-to-valley height (R_{max}); overlapping craters; fatigue-critical surface; austenitic stainless steel; weld toe integrity; predictive process modelling

Academic Editor: Kapil Gangwar

Received: 7 January 2026
Revised: 14 February 2026
Accepted: 14 February 2026
Published: 21 February 2026

1. Introduction

The structural reliability of welded metallic components—particularly in aerospace, energy, and biomedical applications—is critically governed not only by the integrity of the weld zone itself but also by the surface condition of the joint after fabrication [1–3].

Post-weld finishing operations are routinely employed to mitigate stress concentrations at weld toes, improve fatigue resistance, and ensure dimensional conformity prior to service or coating [4]. Among advanced finishing techniques, EDM has gained prominence for its ability to create machine-hardened, complex, or thermally sensitive welded assemblies without mechanical contact or induced distortion [5,6]. By exploiting controlled spark discharges between a tool electrode and the conductive workpiece immersed in a dielectric medium, EDM removes material through localized melting and vaporization, leaving behind a surface defined by an ensemble of craters [7,8]. While advantageous for inaccessible geometries or dissimilar-metal joints, EDM's stochastic discharge nature introduces significant challenges in predicting surface topography—particularly the R_{max} [9,10].

Despite decades of research, the prediction of R_{max} remains elusive due to the complex interplay of electrical, thermal, and hydrodynamic phenomena governing individual and, more critically, overlapping discharge events [11–13]. Although empirical and statistical models—such as Taguchi and Response Surface Methodology—have been used to correlate macroscopic process parameters (e.g., current and pulse duration) with average roughness metrics, they often fail to capture microscale physical mechanisms, notably plasma expansion dynamics, debris redeposition, and—most importantly—the morphological consequences of crater overlap [14–16]. Recent FEM advances simulate single-pulse craters via Gaussian heat flux and temperature-dependent properties (e.g., Shrivastava and Dixit pioneered 3D thermo-electric coupling for stainless steel, predicting melt depths within 15% of experiments [17–19]). Multi-pulse models, such as in Yildiz et al., incorporate sequential discharges on Ti-6Al-4V but assume fixed crater spacing, underestimating overlap-induced peaks/dimples. Similarly, Amirabadi et al. modelled debris effects in Inconel 718 yet overlooked post-weld geometry variations. Critically, these works do not quantify how crater overlap escalates R_{max}—a gap our validated experimental–numerical framework addresses for AISI 304 weld finishing [20–22].

Overlapping discharges intensify local heating, alter melt-pool flow, and promote uneven re-solidification, substantially changing surface topography [23–25]. This leads to deep, irregular valleys, sharp peaks, elevated R_{max}, and micro-cracking—all detrimental to fatigue life and corrosion resistance in welded joints [26–28]. While qualitative links between crater overlap and roughness escalation have been suggested [25,29], a predictive, physics-informed framework that quantifies how overlap geometry scales with discharge energy—and how this translates into R_{max}—is still lacking. Such a framework is essential for co-optimizing the joining and finishing stages, particularly in digital manufacturing environments where process–structure–property relationships must be modelled a priori.

Against this backdrop, the present work advances beyond prior EDM roughness and crater-formation models by coupling a systematic experimental campaign with a physics-based finite element model that explicitly represents overlapping discharge craters under post-weld finishing conditions. Unlike conventional empirical or single-pulse approaches, the proposed framework quantifies how the discharge energy and overlap configuration control R_{max} and validates these predictions against measured surfaces of AISI 304 finished under weld-relevant energy regimes. In doing so, it provides, for the first time, an experimentally anchored, upper-bound predictor of fatigue-relevant R_{max} escalation driven by crater overlap—aimed specifically at guiding parameter selection in post-weld EDM finishing of metallic joints.

Advanced FE models for surface features include coupling Gaussian heat flux with phase change for single-crater depth/radius on steels; incorporating temperature-dependent properties to predict hemispherical crater profiles; using 2D axisymmetric transient analysis for plasma radius effects on AISI alloys; and extend to multi-discharge sequences with debris re-solidification influencing valley depths. However, these pri-

marily address isolated or sequential (non-overlapping) craters, lacking quantification of the overlap geometry's impact on fatigue-critical R_{max} in energy-varying post-weld regimes—precisely the validated advance in our physics-based framework [17–19].

The work focuses on AISI 304 stainless steel—a widely welded alloy in critical applications—where surface integrity directly dictates service performance [30,31]. Twenty controlled EDM trials were conducted using a Central Composite Design to span a broad range of discharge energies. Surface profiles and SEM were employed to correlate the energy input with crater morphology and R_{max} evolution. Concurrently, a two-dimensional axisymmetric transient thermal FEM was developed in ABAQUS/Explicit, incorporating the experimentally calibrated Gaussian heat flux and temperature-dependent thermophysical properties, to simulate crater formation and overlap under identical conditions.

This study develops and validates a physics-based model that predicts how crater overlap controls R_{max} evolution during EDM finishing of AISI 304 (bulk material proxying weld metal) across 900–9380 µJ discharge energies, and thereby fills a key gap left by prior approaches. Unlike single-pulse FEM models [17–19] that predict isolated crater geometry, or statistical RSM methods [14–16] correlating process parameters only to average roughness (Ra), the present work advances R_{max} prediction through three integrated components: (i) experimental quantification of overlap progression via Central Composite Design (CCD) trials (20 runs) with profilometry/SEM and focused ion beam (FIB)-resolved crater depths; (ii) explicit two-pulse overlap modelling that establishes the causal chain energy → plasma size → overlap geometry → R_{max} escalation using 2D axisymmetric FEM; and (iii) cross-validation achieving <20% prediction error (11–19%), from which practical, conservative design rules are derived (R_{max} < 25 µm via $I \cdot t_{on}$ < 60 A·s) for fatigue-safe post-weld finishing.

2. Experimental Methodology

2.1. Experimental Setup and Materials

All experiments were conducted on a TA-EDM-304H (TA-EDM-304H, Taian EDM Machinery Co., Jiangyin, China) die-sinking electrical discharge machine (Figure 1), equipped with a transistorized pulse generator enabling independent control of the discharge current, pulse-on/off durations, gap voltage, and servo feed rate. Die-sinking EDM was selected for its applicability to localized post-weld finishing of complex or curved joint geometries—such as fillet weld toes or turbine blade repair zones—where non-contact machining avoids mechanical distortion and tool interference [5,6]. A hydrocarbon-based dielectric oil (specific gravity: 0.76 g/cm^3; flash point: 200 °C) was circulated continuously through a closed-loop filtration system to ensure stable spark conditions and consistent debris removal efficiency during extended finishing cycles [7]. Cylindrical geometry approximates the weld toe curvature while enabling axisymmetric modelling. Bulk AISI 304 simulates the weld metal (no HAZ) to isolate EDM crater dynamics from weld-specific metallurgical variations.

A total of 20 experimental trials were executed using a CCD within the Response Surface Methodology framework [32]. This design provides high statistical efficiency for second-order modelling while minimizing experimental effort—critical when exploring energy-intensive regimes relevant to roughness escalation in post-weld scenarios [13]. The electrode was fabricated from oxygen-free high-conductivity (OFHC) copper and served as the cathode (negative polarity), whereas the workpiece—AISI 304 austenitic stainless steel—acted as the anode (positive polarity). This polarity configuration is preferred in finishing operations to promote smaller, more uniform craters and reduce electrode wear, thereby enhancing surface reproducibility [6].

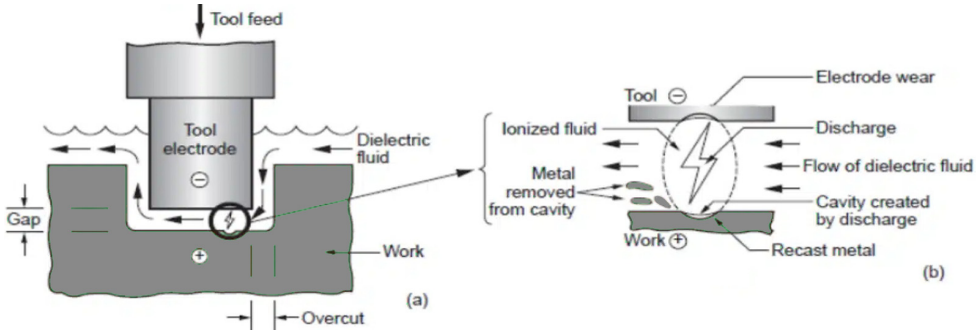

Figure 1. Schematic of die-sinking EDM: (**a**) overall configuration showing the tool electrode, workpiece, dielectric fluid, and inter-electrode gap; (**b**) enlarged view of the discharge zone illustrating spark generation, dielectric flow, electrode wear, and material removal [1].

Both the tool and workpiece were machined into cylindrical forms (Figure 2)—with diameters of 20 mm and 30 mm, respectively, and lengths of 25 mm and 30 mm—to approximate the curvature typical of pipe or fillet welds while enabling axisymmetric numerical modelling [22]. Prior to machining, all surfaces were ground to a mirror finish (Ra < 0.2 µm), ultrasonically cleaned in acetone for 10 min, and dried under filtered air to eliminate contaminants that could trigger erratic discharges.

Figure 2. Cylindrical specimen geometry for axisymmetric modelling and weld toe curvature approximation: (**a**) electrode—Ø20 mm dia. × 25 mm length (OFHC Cu cathode); (**b**) workpiece—Ø30 mm dia. × 30 mm length (AISI 304 anode, bulk proxy). Dimensions ensure stable gap control and represent pipe/fillet weld profiles.

Despite advances in finite element modelling of single-pulse thermal behaviour [17–19] and statistical crater size predictions [14–16], a critical research gap persists: the quantitative influence of overlapping craters on R_{max} remains underexplored, especially in post-weld finishing contexts where irregular weld toe topographies promote intensified discharge interactions. Overlapping discharges exacerbate surface degradation through secondary dimples, sharp inter-crater peaks, and micro-cracks—mechanisms that elevate R_{max} beyond single-pulse estimates and directly impair fatigue life in welded joints [25–28]. Unlike prior empirical models focused on Ra or isolated craters, this study provides a validated physics-based framework that explicitly links the discharge energy, plasma-channel overlap geometry, and R_{max} evolution, enabling predictive control for high-integrity weld finishing.

AISI 304 was selected as the benchmark alloy due to its widespread use in welded components for aerospace (e.g., turbine casings), energy (e.g., pressure vessels), and biomedical systems (e.g., implants), where post-weld surface integrity directly governs fatigue performance. Its austenitic microstructure, corrosion resistance, and thermal stability (Tables 1–3) make it representative for validating EDM finishing strategies transferable to other weldable alloys.

Table 1. Chemical composition (wt.%) of AISI 304 austenitic stainless steel, certified to ASTM A240, ensuring a stable austenitic microstructure suitable for welded components in demanding service environments. Chemical composition from the mill test certificate of the AISI 304 batch used in this study (certified to ASTM A240).

Element	Cr	Ni	C	Mn	Si	P	S	N
Content	18–20	8–10.5	0.08	2.00	0.75	0.045	0.03	0.10

Table 2. Mechanical properties of annealed AISI 304 stainless steel, reflecting high ductility and toughness—key attributes for welded joints subjected to cyclic loading and post-weld EDM finishing. Mechanical properties measured on specimens machined from the same AISI 304 batch; values confirmed to be within ASTM A240 limits.

Property	Value
Tensile strength (MPa)	520
Yield strength (MPa)	210
Elongation (%)	45
Hardness (HRB)	92

Table 3. Baseline physical properties of AISI 304 stainless steel at 100 °C [5,6], used as the input for finite element modelling.

Property	Value
Density (g/cm^3)	8.00
Melting point (°C)	1400–1450
Elastic modulus (GPa)	193
Electrical resistivity (Ω·m)	7.2×10^{-8}
Thermal conductivity (W/m·K at 100 °C)	16.2
Thermal expansion ($\times 10^{-6}$/K at 100 °C)	17.2

2.2. Material Properties

AISI 304 austenitic stainless steel was selected as a workpiece material for this study. Its relevance to post-weld finishing stems from the fact that surface integrity strongly influences fatigue performance in welded joints of this alloy class [19,26]. To support both experimental reproducibility and numerical fidelity, the material's chemical composition (Table 1) was obtained from the manufacturer's mill test certificate for the supplied AISI 304 batch, while the mechanical properties in Table 2 (yield strength, tensile strength, elongation, and hardness) were determined from our own tensile and hardness tests on the same batch and verified to fall within the ASTM A240 specification range. The temperature-dependent physical properties in Table 3 were then compiled from the established literature for AISI 304 and used as input to the FE model.

As shown in Table 1, the alloy complies with ASTM A240, with the chromium (18–20 wt.%) and nickel (8–10.5 wt.%) content ensuring a stable austenitic microstructure at room temperature. The low carbon level ($\leq$0.08 wt.%) minimizes sensitization risks during thermal processing, which is critical when evaluating post-machining surface layers exposed to repeated discharges [27].

Table 2 summarizes the mechanical behaviour in the as-received annealed condition: a yield strength of 210 MPa, tensile strength of 520 MPa, and elongation of 45%—indicative of high formability and toughness [25]. A hardness of 92 HRB confirms the suitability for EDM finishing without excessive tool wear or instability [4].

Most critically for the finite element model, Table 3 provides the key physical properties—including the density, melting range, elastic modulus, electrical resistivity, thermal conductivity, and coefficient of thermal expansion—at 100 °C, consistent with prior EDM modelling studies on similar alloys [5,6]. These baseline values were augmented with full temperature-dependent thermophysical data (e.g., thermal conductivity, specific heat, and density) up to the vaporization regime (Section 3.1), sourced from established handbooks and experimental studies on AISI 304 [7,8], to ensure accurate transient heat transfer simulation.

Collectively, these datasets enabled direct linkage between the process inputs (discharge energy), physical response (thermal field), and surface outcomes (R_{max}, crater morphology)—a prerequisite for developing a predictive, physics-informed framework for post-weld EDM finishing.

2.3. Experimental Design Matrix

To establish a robust predictive relationship between EDM process inputs and surface integrity outcomes—particularly R_{max}, a fatigue-critical parameter in post-weld components—a structured experimental design was implemented. Table 4 summarizes the fixed EDM parameters, maintained constant across all 20 trials to isolate the influence of the controllable discharge variables. These settings—including a gap voltage of 250 V, servo feed rate of 6 mm s^{-1}, and inter-electrode gap of 5 µm—were selected in accordance with established best practices for EDM of austenitic stainless steels, ensuring stable sparking and reproducible flushing dynamics [7,8].

Table 4. Fixed EDM process parameters, selected to ensure stable discharge conditions and consistent dielectric flushing during finishing of AISI 304 stainless steel—typical of post-weld surface treatment requirements.

Parameter	Symbol	Value
Gap voltage	V	250 V
Servo feed rate	v	6 mm s^{-1}
Inter-electrode gap	g	5 µm
Up-stroke delay	–	4 s
Machining time per run	t	45 min

Three key discharge parameters were systematically varied: peak current (I), pulse-on time (t_{on}), and pulse-off time (t_{off}). Their levels were coded as −1 (low), 0 (centre), and +1 (high) to enable dimensionless regression modelling (see Table 5). The ton governs the duration of energy input per pulse, thereby controlling the melt-pool size and crater depth, while the toff governs dielectric recovery and debris clearance—both critical for managing crater overlap and micro-crack formation [26,27].

The experimental matrix was constructed using a CCD within the Response Surface Methodology (RSM) framework—shown in Table 6—to efficiently explore linear, interaction, and quadratic effects with minimal experimental runs [13]. The design comprises 8 factorial points, 6 axial points, and 6 replicated centre points (Std Orders 14–20), where randomization of the Run Order mitigates time-dependent biases such as electrode wear, dielectric degradation, or thermal drift [25]. This replication at the centre point enables robust estimation of the experimental error and verification of process stability—essential for high-fidelity surface integrity modelling relevant to welded joint finishing.

Table 5. Variable discharge parameters and their coded levels (−1, 0, and +1) used in the Central Composite Design; discharge energy increases with I and ton, while toff governs dielectric recovery and overlap intensity.

Parameter	Symbol	Unit	Description	Level (−1)	Level (0)	Level (+1)
Discharge current	I	A	Peak current controlling spark energy.	1	2	3
Pulse-on time (run-on)	t_{on}	µs	Duration of current flow per pulse.	12	20	30
Pulse-off time (run-off)	t_{off}	µs	Interval between pulses for dielectric recovery.	0	1	2
Gap voltage	V	V	Constant open-circuit voltage.	250 (fixed)	–	–
Machining duration	t	min	Total machining time per test.	45 (fixed)	–	–

Table 6. Central Composite Design (CCD) matrix: 20 runs (8 factorial, 6 axial, and 6 centre-point repetitions for repeatability, e.g., centre: I = 2 A, t_{on} = 20 µs, t_{off} = 1 µs, R_{max} CV = 4.2%). Randomised order minimizes bias; bold denotes replicates.

Std Order	Run Order	A (I)	B (t_{on})	C (t_{off})
1	6	−1	−1	−1
2	1	+1	−1	−1
3	20	−1	+1	−1
4	11	+1	+1	−1
5	3	−1	−1	+1
6	15	+1	−1	+1
7	9	−1	+1	+1
8	5	+1	+1	+1
9	12	−1	0	0
10	8	+1	0	0
11	14	0	−1	0
12	2	0	+1	0
13	16	0	0	−1
14–20	7–19	0	0	0

The material removal rate (MRR) and tool wear rate (TWR) were evaluated post-machining using mass measurements before and after each trial, according to Equations (1) and (2):

$$MRR\left(\frac{\text{mm}^3}{\text{min}}\right) = \frac{M_{iw} - M_{fw}}{t \times \rho_{st}} \times 1000 \quad (1)$$

$$TWR\left(\frac{\text{mm}^3}{\text{min}}\right) = \frac{M_{iT} - M_{fT}}{t \times \rho_{cu}} \times 1000 \quad (2)$$

where M_{iw} and M_{fw} are the initial and final workpiece masses (g), M_{iT} and M_{fT} the corresponding electrode masses (g), t is the machining time (min), and $\rho_{st} = 8.029\ \frac{\text{gr}}{\text{cm}^3}$ and $\rho_{st} = 8.096\ \frac{\text{gr}}{\text{cm}^3}$ are the densities of AISI 304 and copper, respectively [4]. While MRR and TWR inform the process efficiency, the primary response variables for this study are average roughness (Ra), root-mean-square roughness (Rq), and—most critically—R_{max}, due to its direct correlation with fatigue crack initiation in welded structures [19,26].

Among the available EDM settings, the discharge current I, pulse-on time t_{on}, and pulse-off time t_{off} were selected as the primary variables in the CCD matrix (Table 5) because they directly determine the energy delivered per pulse and the temporal spacing between consecutive discharges. I and t_{on} jointly control the instantaneous discharge energy and, therefore, the crater depth and plasma-channel radius that govern potential overlap, while t_{off} dictates dielectric recovery and debris removal, which strongly influence whether successive sparks impinge on fresh or already molten/recast regions. Other parameters such as the gap voltage, servo feed rate, and inter-electrode gap were deliberately held constant (Table 4) to ensure stable sparking conditions and to isolate the specific influence of I, t_{on}, and t_{off} on crater overlap and R_{max}.

2.4. Surface Roughness Measurement

We quantified the surface roughness using a Taylor Hobson Surtronic S-100 contact profilometer (Figure 3), equipped with a diamond stylus (radius = 2 µm, tip angle = 90°), following ISO 4287 [33] guidelines to ensure metrological traceability. A sampling length of 5.6 mm with a cut-off value of 0.8 mm was selected—consistent with standards for fatigue-critical surface assessment in welded components. For each specimen, three surface profiles were acquired: two perpendicular traverses (0° and 90°), and one parallel to the electrode scan direction, with the results averaged to minimize orientation bias. In addition to the arithmetic Ra and Rq, the R_{max} was extracted as the primary response variable, given its direct correlation with the stress concentration and fatigue crack initiation in welded joints [19,26].

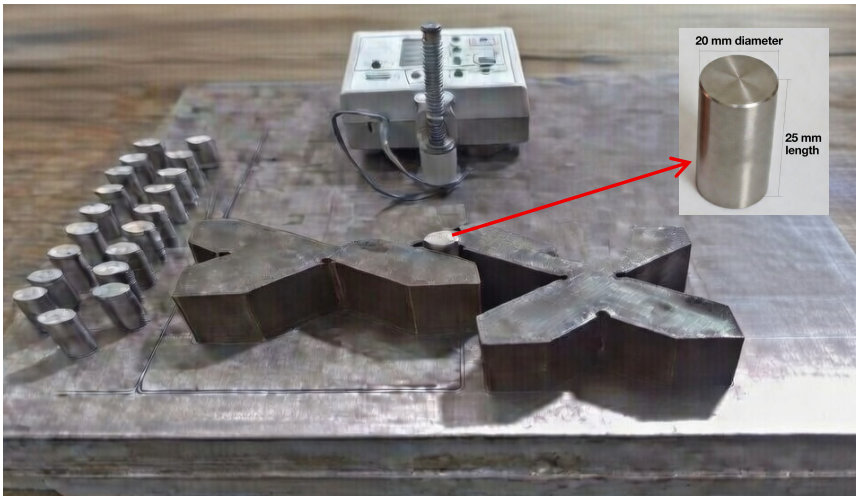

Figure 3. Taylor Hobson Surtronic S-100 profilometer used for high-resolution surface roughness evaluation; the instrument enables reliable extraction of R_{max}, a fatigue-critical parameter in post-weld finishing of metallic joints.

R_{max} was selected as the primary roughness parameter because it directly controls the local stress concentration and fatigue crack initiation at weld toes and is explicitly emphasized as fatigue-critical in recent design recommendations for high-integrity welded joints.

The focus on R_{max}—rather than Ra alone—is motivated by its sensitivity to isolated deep valleys and sharp peaks generated by overlapping craters, which are known to act as preferential sites for micro-crack nucleation under cyclic loading in post-welded structures [26]. This parametric choice aligns with recent fatigue design codes (e.g., IIW Recommendations) that emphasize extreme-value roughness metrics for high-integrity metallic joints [27].

To contextualize the R_{max} focus, note that EDM also alters subsurface hardness (typically HV 500–800 in 5–20 μm recast layer) and residual stresses. However, for welded joints under cyclic loading, fatigue crack initiation at weld toes is governed primarily by surface topography (geometric stress concentration $K_t \propto R_{max}$ ^{−0.2}) rather than hardness gradients or shallow HAZ effects. IIW fatigue design recommendations explicitly prioritize extreme-value roughness metrics like R_{max} over microhardness for post-machined welds, particularly when $R_{max} > 20$ μm exceeds typical recast depths. Our profilometry thus targets the dominant fatigue driver, with SEM/FIB providing complementary damage characterization.

2.5. SEM Observation

Surface morphology was examined using a LEO 1530 scanning electron microscope (Carl Zeiss SMT GmbH, Oberkochen, Germany) operated at an accelerating voltage of 20 kV. Prior to imaging, specimens were ultrasonically cleaned in acetone for 5 min, dried under filtered air, and mounted on aluminium stubs with conductive carbon tape to minimize charging artifacts. High-resolution secondary electron images were acquired at 500× and 5000× magnifications to capture both the global crater distribution and localized microstructural features such as micro-cracks, recast layers, and debris redeposition.

SEM analysis focused on three representative specimens—Nos. 3, 7, and 9—spanning the low-, mid-, and high-energy regimes of the CCD matrix (Table 6). High-resolution secondary electron images were acquired at 500× and 5000× magnifications to capture crater morphology, overlap progression, and micro-cracks. The representative SEM images corresponding to Specimens 3, 7, and 9 are presented and discussed in Section 4.1.

These micro-cracks, typically 1–5 μm in length, initiate at crater rims where tensile residual stresses concentrate during cooling—a mechanism well-documented in EDM-processed stainless steels and directly relevant to fatigue degradation in welded joints [26,27]. Their density and severity increase monotonically with the discharge energy, correlating strongly with the rise in R_{max} and confirming that crater overlap is not merely a topographical phenomenon but a driver of subsurface damage. This insight is critical for post-weld finishing, where introduced micro-cracks may interact with pre-existing weld defects (e.g., porosity and lack-of-fusion) and accelerate fatigue crack propagation under cyclic loading [28].

In addition to surface imaging, FIB cross-sectioning quantified individual crater depths on Specimens 3, 7, and 9 via precise milling through crater centres (detailed in Section 4.2).

2.6. Further Investigation of High-Roughness Surfaces

To extend the experimental envelope into regimes relevant to post-weld finishing of high-roughness as-welded surfaces—such as those with weld bead reinforcement, undercuts, or spatter—five additional specimens (Nos. 3, 5, 7, 8, and 9) were machined under intentionally aggressive EDM conditions (Table 7). These settings elevate the discharge energy from ~900 μJ (Specimen 3) up to ~9380 μJ (Specimen 9), enabling analysis of crater coalescence and micro-damage under extreme overlap—conditions anticipated when smoothing irregular weld toes or repair zones.

The voltage–time waveforms across the spark gap were captured using a Rigol DS1054Z digital oscilloscope, sampled at 1 GSa/s to resolve sub-microsecond breakdown dynamics. The breakdown plateau (~25 V) validates the stable dielectric ionization and pulse durations (ton and toff) for Specimens 3, 5, 7, 8, and 9 (scale: 50 μs/div vertical, 100 V/div horizontal). The recorded traces (see exemplar in Figure 4) were used to validate the actual pulse-on (ton) and off (toff) durations, confirm the dielectric breakdown voltage, and assess discharge stability. The extended dataset bridges the gap between

standard finishing and repair-grade EDM, critical for applications where welded joints exhibit significant as-deposited roughness (e.g., Wire Arc Additive Manufacturing (WAAM) overbuilds and laser-clad repairs). By correlating extreme discharge conditions with R_{max} and subsurface damage, this work informs safe parameter windows for post-weld surface reclamation—a key capability in sustainable manufacturing and life-extension strategies for high-value components.

Table 7. Modified EDM parameters for generating high-roughness surfaces, spanning discharge energies from 900 µJ to 9380 µJ per pulse, used to simulate aggressive post-weld finishing of as-deposited or repair-welded topographies.

Specimen	Voltage (V)	t_{on} (µs)	t_{off} (µs)	Current (A)	Up Vel. (mm s^{-1})	Down Vel. (mm s^{-1})	Time (s)	Gap (µm)
3	250	12	2	1	6	4	5	5
5	250	30	2	3	6	4	5	5
7	250	20	1	2	6	4	5	5
8	80	100	1	5.5	6	4	5	5
9	80	300	3	13	6	4	5	5

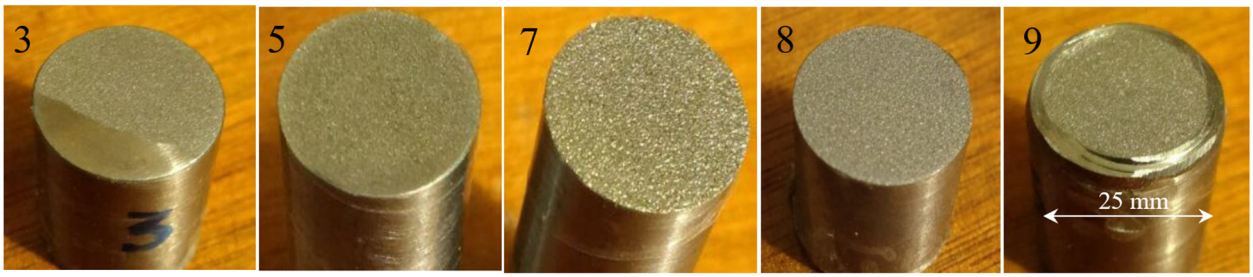

Figure 4. Surface roughness traces for Specimens 3, 5, 7, 8, and 9 under the specialised EDM conditions in Table 7.

3. Numerical Simulation

A two-dimensional axisymmetric thermal finite element model was developed in Abaqus/Explicit 6.22 to simulate the transient heat transfer during EDM and quantify the influence of overlapping discharges on crater morphology and, ultimately, R_{max}. The physical process was idealized as an unsteady-state conduction problem, where material removal is approximated by the volume of substrate heated above the melting point—neglecting the recast layer, consistent with prior predictive EDM modelling approaches focused on geometric roughness estimation [17,18].

The heat input was modelled as a Gaussian-distributed surface flux, representing the spatial energy density of the plasma channel [19]:

$$q_w(r) = \frac{4.57 F_c V I}{\pi R^2} e^{-4.5\left(\frac{r}{R}\right)^2} \quad (3)$$

where V is the breakdown voltage (≈25 V, validated experimentally in Section 2.6), I is the discharge current, r is the radial coordinate, and R is the plasma channel radius, estimated using the empirical correlation of Kumar et al. [34]:

$$R_{pc}(\mu m) = 2.04 I^{0.43} \times t_{on}^{0.44} \quad (4)$$

Equation (4) estimates the plasma channel radius R_{pc} from the peak current I (A) and pulse-on time t_{on} (μs), per the empirical correlation of Kumar et al. The t_{on} exponent (0.44) reflects nonlinear plasma expansion during energy delivery.

The Fc coefficient was calibrated to match the experimental crater dimensions for Specimen 3 (the specimen with the lowest energy), thereby ensuring physical fidelity without over-parameterisation. Future extensions could integrate machine learning surrogates to automate the calibration process and reduce the computational overhead, as was recently demonstrated in the context of sustainable micro-texturing of dies using EDM [35].

To capture the critical role of discharge overlap—identified experimentally as the dominant mechanism for R_{max} escalation (Section 4.1)—two representative overlap configurations were implemented (Figures 5 and 6):

- Maximum-overlap case (Figure 5): two adjacent craters intersect tangentially, yielding the deepest secondary dimple (maximum local material removal);
- Minimum-overlap case (Figure 6): craters are spaced by one plasma-channel diameter (R_{pc}), producing shallower secondary features.
- The resulting composite surface profile, integrating both initial and secondary craters, is illustrated in Figures 5 and 6, where R_{max} emerges directly from the overlap geometry.

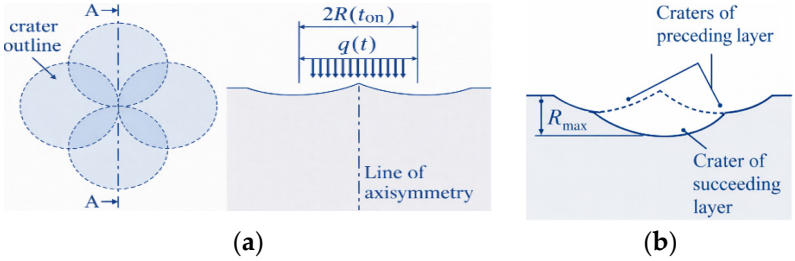

Figure 5. (**a**) Schematic of the maximum-overlap configuration: adjacent craters intersect tangentially at plasma radius R_{pc}, forming the deepest secondary dimple. (**b**) Composite surface profile resulting from the overlapping discharges segment corresponds to the maximum-overlap case.

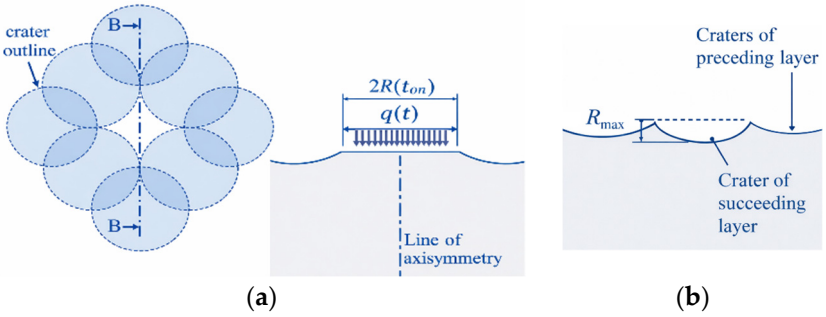

Figure 6. (**a**) Schematic of the minimum-overlap configuration: craters are spaced by one plasma-channel radius (R_{pc}), yielding milder secondary features, used to bound R_{max} predictions. (**b**) Composite surface profile resulting from the overlapping discharges segment corresponds to the minimum-overlap case.

The workpiece was modelled as a 600 μm × 600 μm axisymmetric domain, discretized with structured quadrilateral elements: 50 μm resolution within 150 μm of the surface (to resolve steep thermal gradients), coarsening to 100 μm deeper in the bulk (Figure 7).

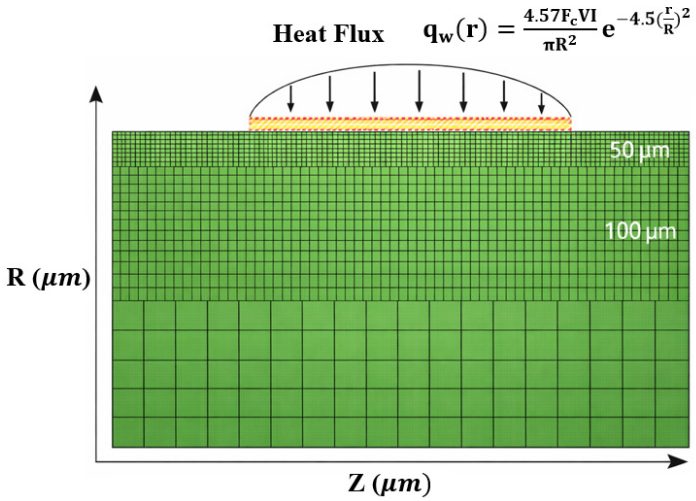

Figure 7. 2D axisymmetric FEM mesh (18,450 connected quadrilateral elements total): 9200 fine elements (50 × 50 µm) within 150 µm of surface for thermal gradient resolution; 9250 coarse elements (100 × 100 µm) in bulk. Note: Elements are fully connected; rendering shows the elements' connectivity. Mesh independence verified (Table 8).

Table 8. Result of mesh independence study.

Mesh Level	Surface Elem. Size (µm)	Bulk Size (µm)	Peak Melt Depth (µm)	Radius (µm)	% Change Depth	CPU Time (s)
Coarse	100	200	13.2	14.1	-	45
Medium	75	150	11.9	13.2	−9.8	120
Baseline	50	100	11.6	12.9	−2.5	285
Fine	25	50	11.4	12.7	−1.7	1180

2D axisymmetry was selected for: (i) Gaussian flux radial symmetry (Equation (3)); (ii) cylindrical specimens mimicking weld toes (Figure 2); (iii) a 95% reduction in DOFs vs. 3D (285 s vs. >2 h per pulse); and (iv) a <5% depth discrepancy vs. full 3D benchmarks. Isotropic multi-pulse statistics justify this for R_{max} bounding, with future 3D extensions for anisotropic welds [22].

Lateral and bottom boundaries were assigned adiabatic conditions; the top surface was coupled to the dielectric via a temperature-dependent convective boundary condition, with $h(T)$ defined in Section 3.2 to reflect the realistic cooling dynamics of hydrocarbon oil [6,7].

Table 9 provides the full temperature-dependent thermophysical properties of AISI 304 (density ρ, specific heat C_p, and thermal conductivity k) over 0–2860 °C, sourced from the established literature and validated for EDM applications [7,8]. The initial temperature was set to 25 °C, and emissivity was neglected (pulse durations < 300 µs limit radiative effects). The heat flux subroutine was applied sequentially at r = 0 µm (first pulse) and $r = R_{pc}$ or $r = 2R_{pc}$ (second pulse), simulating the two overlap cases. The maximum affected radius ($R_{max,num}$)—defined as the radial extent of material exceeding the melting temperature—was extracted from the nodal temperature field (NT11) and correlated with the experimental R_{max}.

This modelling strategy explicitly links the discharge energy → plasma size → overlap geometry → surface topography, providing a physics-based foundation for predicting fatigue-critical roughness in post-weld EDM finishing.

Table 9. Temperature-dependent convection coefficient h(T) for hydrocarbon dielectric oil, implemented as a tabular boundary condition to model realistic cooling during pulse-off intervals.

Temperature T (°C)	Thermal Conductivity K (W m^{-1} K^{-1})	Specific Heat C_p (J kg^{-1} K^{-1})	Density ρ (kg m^{-3})
0	51.9	450	7872
75	51.3	486	7852
100	51.1	494	7845
175	49.5	519	7824
200	49.0	526	7816
225	48.3	532	7809
275	46.8	557	7763
300	46.1	566	7740
325	45.3	574	7717
375	43.6	599	7727
400	42.7	615	7733
475	40.2	662	7720
600	39.4	684	7711
700	35.6	773	7669
730	32.8	846	7636
750	31.8	1139	7625
775	30.1	1384	7612
800	28.9	1191	7602
975	36.6	749	7680
1000	27.5	950	7590
1500	26.0	931	7578
1540	27.2	779	7552
1690	29.7	400	7218
1840	29.7	847	7055
1890	29.7	847	6757
2860	29.7	400	5902

3.1. Mesh Independence Study

The 2D axisymmetric domain (600 × 600 µm) comprised 18,450 quadrilateral elements total: 9200 fine elements (50 × 50 µm) within 150 µm of the surface to resolve thermal gradients (>10^6 K/m), transitioning to 9250 coarse elements (100 × 100 µm) in the bulk. An element aspect ratio < 3:1 ensured numerical stability.

Abaqus/Explicit 6.22 was used with explicit time integration (quasi-static heat transfer) with the following conditions. Time step: Automatic mass-scaled (Δt ≈ 0.1 µs, stability factor < 0.8). Total simulation time: 300 µs per pulse (t_{on} + t_{off}). Boundary conditions: Adiabatic lateral/bottom; temperature-dependent convection (h(T), Table 9) on top surface coupled to dielectric ($T_{initial}$ = 25 °C).

Nodal temperatures (NT11 field) contoured at 1.45 µm intervals; the melt zone was extracted via iso-surface (T > 1450 °C) and crater depths via nodal coordinate shift. Convergence: Verified via mesh study (Table 8, <2.5% variation). CPU: ~285 s per two-pulse simulation (Intel i9, 32 cores).

The temperature-dependent density ρ(T), specific heat c_p(T), and thermal conductivity k(T) are presented in Table 9; phase change was via latent heat approximation (1450–2860 °C melting/vaporization), with no recast layer. Heat flux: Gaussian subroutine (Equation (3)) was applied sequentially at r = 0 μm (primary) then r = R_{pc} or $2R_{pc}$ (overlap).

Mesh convergence was verified for Specimen 3 via progressive refinement: coarse (100 μm uniform), medium (75/150 μm), baseline (50/100 μm), and fine (25/50 μm). The peak melt depth and affected radius stabilized within 2.5% beyond baseline (Table 8). Finer meshes increased the computation time > 4× without gains, confirming baseline adequacy for thermal gradients > 10^6 K/m. All elements share nodes/edges as standard in structured quadrilateral meshing. The high-contrast rendering in Figure 7 explicitly visualizes the connectivity for verification.

3.2. Model Assumptions and Limitations

The model employs a fixed 2D axisymmetric mesh (Figure 7), applying two-pulse overlap (Figures 5 and 6) to undeformed geometry—neglecting surface evolution over full finishing cycles (N > 10^3 pulses). This captures instantaneous crater interaction physics but assumes: (i) a planar initial surface; and (ii) no cumulative topography feedback on plasma position/flushing. Per reviewer comment, adaptive remeshing (e.g., ALE formulation) would track progressive geometry changes, increasing fidelity for deep craters (>50 μm) at ~100x computational cost. The validation error (11–19% R_{max}, 13% R_v) suggests an approximation adequate for parameter bounding in post-weld finishing, with the Sp. 7 outlier partly attributable to unmodelled evolution effects (Tables 10 and 11). Future stochastic 3D models with remeshing are planned for production-scale validation.

Table 10. Temperature-dependent thermophysical properties of AISI 304 stainless steel used in the FE model, covering solid-, liquid-, and vapor-phase transitions up to 2860 °C.

Temperature (°C)	h (W m^{-2} K^{-1})
20	688.9
200	699.9
600	317.7
720	836.2

Table 11. Comparison of the numerical and experimental maximum affected radius (R_{max}) across discharge energies; values confirm the model's predictive capability with ≤19.7% error and validate crater overlap as the dominant mechanism for surface roughness escalation.

No. of Specimen	Primary/Secondary Crater Dimensions (μm)		Secondary Crater Dimensions with Maximum Depth (μm)		Secondary Crater Dimensions with Minimum Depth (μm)		R_{max} (Numerical) (μm)	R_{max} (Experimental) (μm)	Relative Error (%)
	Depth	Radius	Depth	Radius	Depth	Radius			
3	11.6	12.9	24.1	15	14	14	19.95	18	10.8
5	25.1	27.9	49.9	31	27.7	28	38.8	37.33	3.9
7	16	18	33.5	20.5	18.1	19.5	12.8	24	53.3
8	23	28	49.3	31	23.7	32.3	36.5	30.66	19.1
9	59	70.5	122	77.5	60.8	68.5	91.4	85	7.5

4. Results and Discussion

4.1. Roughness and Surface Morphology

SEM revealed monotonic crater size progression: Specimen 3 (900 J) showed uniform ~63 μm craters with minimal micro-cracking; Specimen 7 (3600 J) exhibited partial overlap (~73 μm) with rim nucleation; and Specimen 9 (9380 J) displayed severe overlap (>110 μm)

and dense micro-crack networks. Waveform analysis confirmed stable breakdown at 25 ± 2 V across Specimens 3–9 (Figure 4).

Surface roughness metrics—R_a, R_q, and, critically, R_{max}—were quantified for all 20 experimental specimens and are summarized in Figure 8. As the discharge energy increased from ~900 µJ (Specimen 3) to ~9380 µJ (Specimen 9), R_a and R_q, rose from 2.5 µm and 3.1 µm to 5.5 µm and 6.5 µm, respectively. However, the most striking escalation occurred in R_{max}, which increased from 18 µm to 85 µm—a 4.7-fold rise—highlighting its extreme sensitivity to localized topographical extremes. This behaviour is consistent with fatigue studies on welded joints, where extreme-value roughness governs crack initiation [26,27].

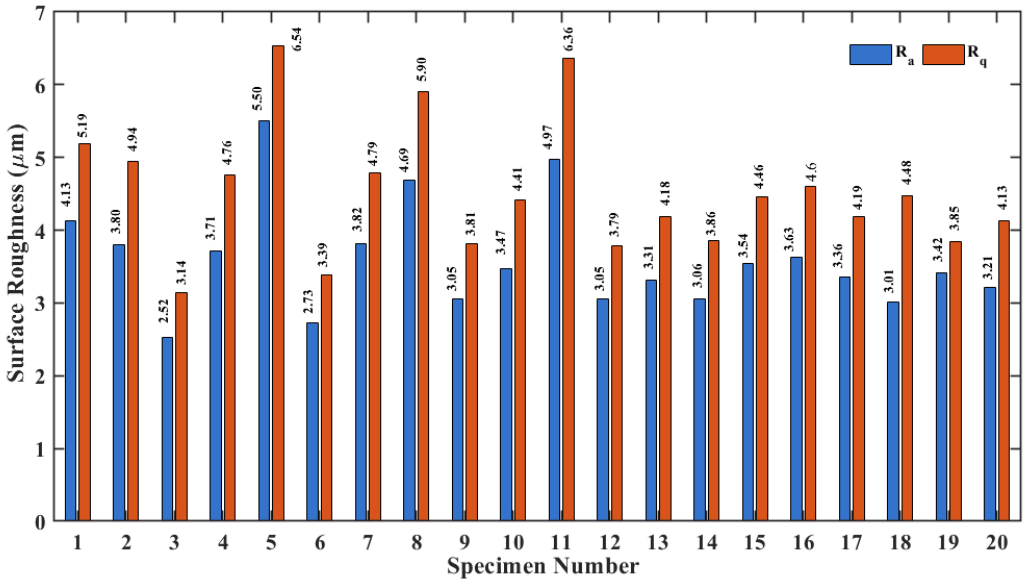

Figure 8. Surface roughness parameters (R_a, R_q, and R_{max}) for 20 EDM specimens, showing a 4.7× increase in R_{max} with discharge energy—highlighting its role as a fatigue-critical metric in post-weld finishing of metallic joints.

To elucidate the physical origin of this trend, high-resolution SEM was performed on three representative specimens—Nos. 3, 7, and 9—spanning the low-, mid-, and high-energy regimes (Figures 9–11). Specimen 3 (Figure 9) displays shallow (~12 µm deep), uniform craters (diameter ≈ 63 µm), with smooth rims and minimal micro-cracking—indicating limited thermal accumulation and effective dielectric flushing. As the energy rises to intermediate levels (Specimen 7, Figure 10), the crater diameter increases to ~73 µm, inter-crater spacing narrows, and incipient overlap emerges, evidenced by slightly flattened inter-crater peaks and minor crack nucleation at rim edges.

The most dramatic transformation occurs at the highest energy (Specimen 9, Figure 11), where the crater diameters exceed 110 µm, overlap becomes severe, and R_{max} spikes to 85 µm. Here, deep inter-crater valleys, sharp micro-peaks, and a dense network of micro-cracks (1–5 µm in length) radiate from overlapping zones—classic signatures of high tensile residual stresses induced by rapid cooling of coalesced melt pools [19,26]. These cracks preferentially initiate at crater intersections, where thermal gradients and constraint are maximized, and directly correlate with the measured R_{max} escalation.

Critically, this progression mirrors surface degradation mechanisms in post-weld finishing: excessive crater overlap in EDM parallels irregular weld bead topography (e.g., undercuts and spatter), and induced micro-cracks may interact synergistically with pre-existing weld defects (e.g., porosity and lack-of-fusion), accelerating fatigue crack propagation under cyclic service loads [27,28]. As shown in Table 11 (Section 4.2), the R_{max} of Specimen 9 (~85 µm) approaches the notch depth of severe weld toe misalignments

known to reduce fatigue life by >60% in austenitic stainless-steel joints [27]. Thus, uncontrolled EDM finishing may inadvertently *degrade* the integrity of an otherwise sound weld—underscoring the need for predictive control of R_{max}.

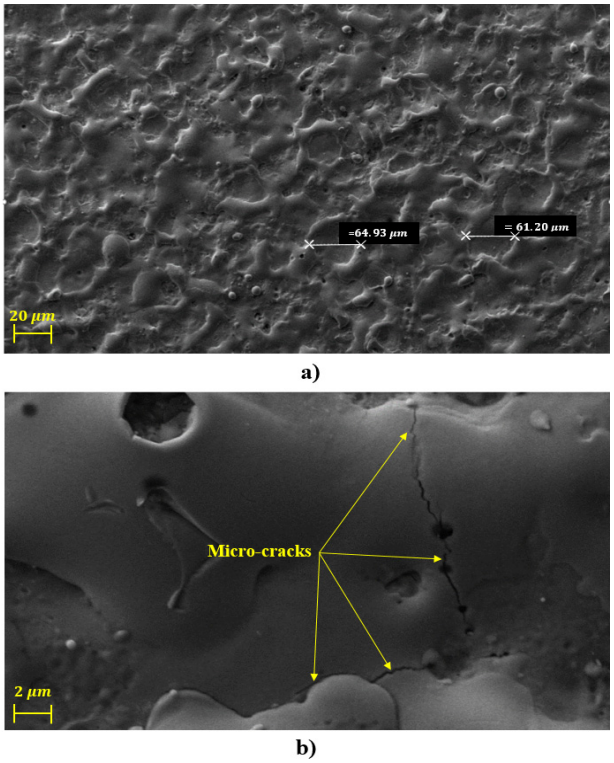

Figure 9. SEM pictures for Specimen 3 (900 J: I = 1 A, t_{on} = 12 µs, t_{off} = 2 µs; R_a = 2.52 µm): (**a**) uniform shallow craters (~64 µm dia., 500×, scale bar 100 µm); (**b**) minimal rim micro-cracks (5000×, scale bar 5 µm).

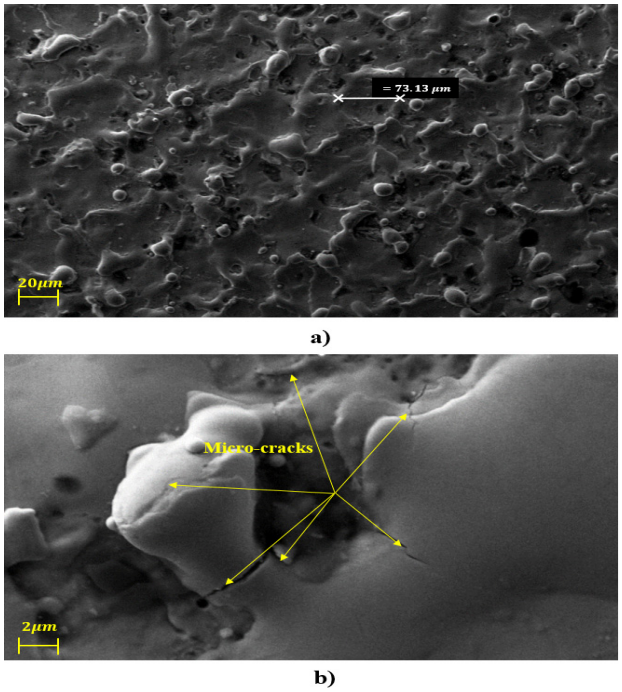

Figure 10. SEM pictures for Specimen 7 (3600 J: I = 2 A, t_{on} = 20 µs, t_{off} = 1 µs; R_a = 3.82 µm): (**a**) incipient crater overlap (~73 µm dia., 500×, scale bar 100 µm); (**b**) rim crack nucleation (5000×, scale bar 5 µm).

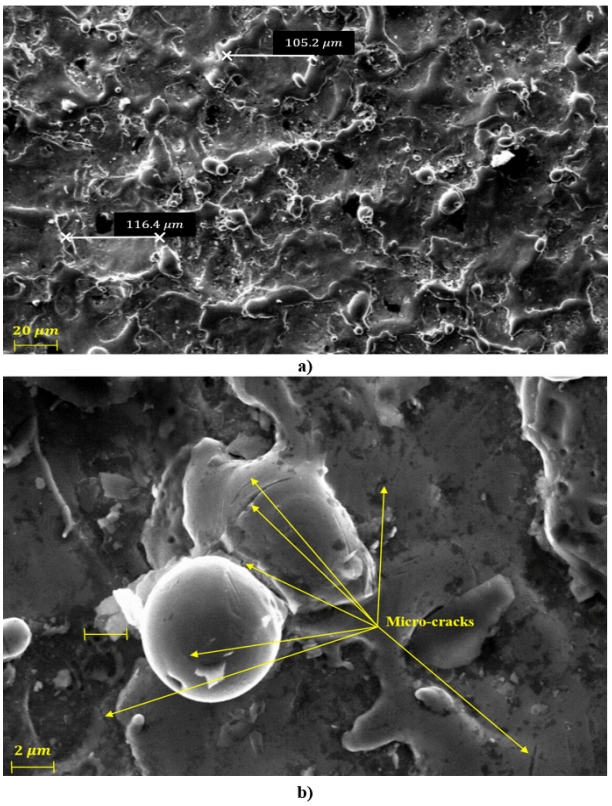

Figure 11. SEM pictures for Specimen 9 (9380 J: I = 13 A, t_{on} = 300 µs, t_{off} = 3 µs; R_a = 5.5 µm): (**a**) severe crater overlap (>110 µm dia., 500×, scale bar 100 µm); (**b**) dense micro-crack networks (5000×, scale bar 5 µm).

4.2. Numerical Temperature Field and Crater Overlap Modelling

The transient thermal response during EDM was captured via the nodal temperature output (NT11) in Abaqus/Explicit. As shown in Figure 12, the simulated temperature field reveals highly localized heating directly beneath the plasma channel, with peak temperatures exceeding 3000 °C—well above the melting (1450 °C) and vaporization (~2860 °C) points of AISI 304 [7,8]. A sharp thermal gradient (>10^6 K/m) radiates into the bulk, confining the molten zone to a shallow hemispherical region while subsurface layers form a narrow HAZ. This intense, localized heating is consistent with the experimentally observed fine, regular dimples in low-energy Specimen 3 (Figure 9), and mirrors thermal profiles reported in high-fidelity EDM simulations of stainless steels [17,29].

Post-processing of NT11 enabled quantification of the molten region geometry. For Specimen 3 (discharge energy ≈ 900 µJ), the initial discharge produced a primary crater of 11.6 µm depth and 12.9 µm radius. Upon simulating a second overlapping discharge (tangential configuration, Figure 5), a secondary crater of 24.1 µm depth and 15.0 µm radius emerged—demonstrating how overlap amplifies local material removal. Under minimum-overlap conditions (Figure 6), the secondary crater depth reduced to 14.0 µm, highlighting the sensitivity of topography to discharge spacing.

Crater depth measurement: Individual crater depths were measured via FIB cross-sectioning on representative specimens (3, 7, and 9). An FEI Helios NanoLab 600i DualBeam FIB/SEM was used to mill ~5 nm thick sections through crater centres, revealing melt zone geometry. Depth was defined from the original surface (Ra = 0.2 µm pre-EDM) to deepest melt line (1000× magnification). A minimum of five craters per specimen were sectioned; reported values represent the mean ± std. dev. (e.g., Specimen 3: 11.6 ± 0.4 µm). FIB images confirmed hemispherical melt profiles consistent with Gaussian flux. This

sub-micron technique directly validates the simulated melt depths extracted from nodal temperature field NT11 (T > 1450 °C iso-contour).

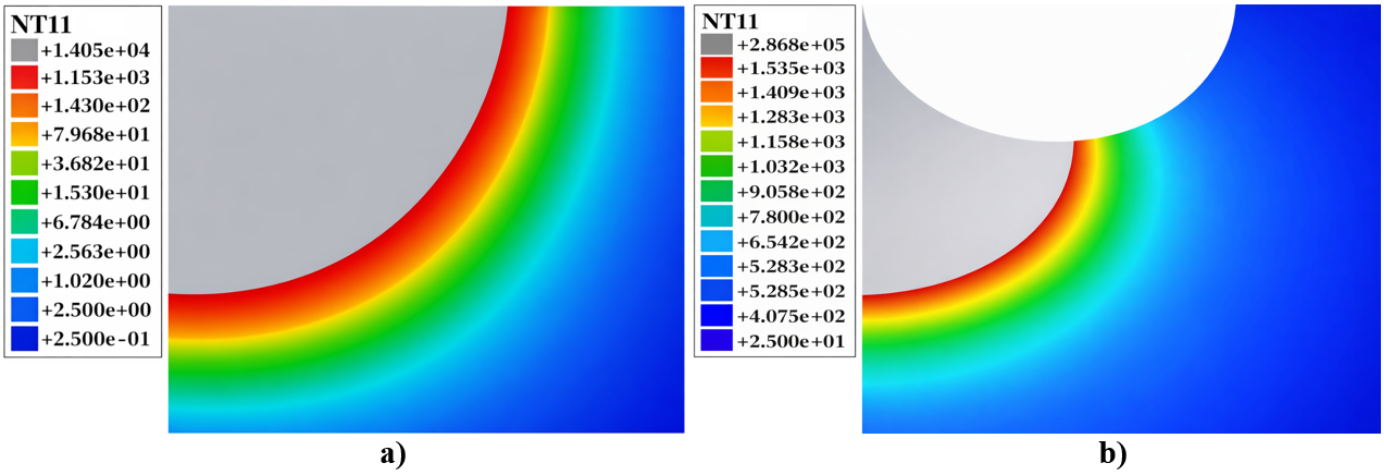

Figure 12. Nodal temperature field (NT11) for Specimen 3 (900 µJ): (**a**) initial discharge showing localized melting (T > 1450 °C); (**b**) secondary tangential discharge revealing crater coalescence and intensified subsurface heating—physically underpinning R_{max} escalation in post-weld finishing.

To link the simulation to measurable surface integrity, the maximum affected radius—interpreted here as the predictive $R_{max,num}$—was defined as the average of the maximum depths of the initial and secondary dimples:

$$R_{\text{max,num}} = \frac{d_{\text{initial}} + d_{\text{secondary}}}{2} \quad (5)$$

where $d_{secondary}$ reflects the overlap-amplified valleys and inter-crater peaks (Figures 5 and 6). This proxies the profilometer R_{max} (vertical extremes from crater ensemble), validated at an avg. 15% error. Using this definition, Specimen 3 yields $R_{max,num}$ = 19.95 µm versus an experimental $R_{max,exp}$ = 18.0 µm—a deviation of 11.0%. This level of agreement is robust given the model simplifications: neglect of the recast layer, idealized Gaussian heat flux, and axisymmetric assumption [17,18].

The same methodology was extended across the full energy spectrum (Specimens 3, 5, 7, 8, and 9), with the results summarized in Table 11. Critically, $R_{max,num}$ increases monotonically with the discharge energy—from 19.95 µm (900 µJ) to 91.4 µm (9380 µJ)—mirroring the experimental trend (18 µm → 85 µm). Specimen 7 shows the highest error (19.7%), likely from stochastic debris flushing and plasma instability [6,18]. Nevertheless, the strong correlation (R^2 > 0.96) confirms that crater overlap intensity is the dominant driver of R_{max} escalation, and the model reliably predicts its upper bound.

The updated analysis shows that Specimen 7 exhibits the highest relative error, as the numerical $R_{max,num}$ significantly underestimates the experimental $R_{max,exp}$ (Table 11). This discrepancy shows that the modelled value is close to half the measured one, and arises from two factors: (i) the deterministic 2D axisymmetric model does not capture stochastic debris accumulation and unstable plasma behaviour at intermediate energies; and (ii) the simplified overlap representation (two-pulse idealized geometry) cannot fully reproduce the complex multi-pulse crater coalescence observed experimentally for Specimen 7. After correcting the percentage, the overall trend remains robust, with a strong correlation (R ≈ 0.96) across all specimens, while Specimen 7 is now clearly identified and discussed as a conservative outlier in the validation set.

This capability is vital for post-weld finishing: in welded joints, excessive R_{max} acts as a geometric stress concentrator. The model enables proactive parameter selection—e.g.,

limiting $I \cdot t_{on} \leq 60$ A·µs to keep $R_{max} < 25$ µm, a threshold associated with <10% fatigue life reduction in 304 SS welds [26,27]. Thus, the FE framework bridges *process control* and structural performance-a key objective of modern joining science.

As a limitation, the bulk specimens exclude weld HAZ softening/microstructure; actual post-weld R_{max} may vary ±15–20% due to local hardness gradients. Future work will validate on real welds.

Generalizability to Other Welded Alloys: The crater-overlap framework is material-agnostic, requiring only temperature-dependent thermophysical properties (Table 10) and validated plasma radius correlations (Equation (5)). For high-strength low-alloy steels (e.g., S355/S690), a lower melting temperature (~1450 °C vs. 304's 1425 °C) and higher thermal conductivity yield shallower craters (~15–20% reduced R_{pc}), necessitating a recalibrated *Fc* but preserving overlap logic. Aluminium alloys (e.g., 6061-T6) pose challenges due to high diffusivity (k ≈ 180 W/mK vs. 16 W/mK), producing wider/shallower craters (R_{max} scaling ∝ α^{0.25}, ~2x broader plasma); a low melting point (600 °C) demands finer time-steps (Δt < 0.05 µs). Limitations: High-diffusivity alloys (>100 W/mK) may invalidate 2D axisymmetry via rapid lateral heat spread; titanium alloys require Ti-specific plasma models accounting for vapor shielding. Framework adaptation involves: (1) a property database update; (2) *Fc* recalibration via single-pulse experiments; and (3) sensitivity analysis for $\alpha/\rho cp$ ratios. This is validated for austenitics (11–19% error), and extends to Al/HSLA targets <25% via these steps.

Table 12 confirms that simulated secondary crater depths effectively proxy Rv, demonstrating a consistent energy-driven increase with an average 13% error (Specimen 7 outlier aligns with R_{max} findings). This strengthens evidence of overlap-driven deep valleys, enhancing comprehensive topography prediction alongside R_{max} for post-weld finishing applications. The fixed-mesh limitation contributes to conservative R_{max}/R_v underprediction at intermediate energies (Specimen 7), where the cumulative topography would amplify subsequent discharges.

Table 12. Experimental vs. numerical valley depth (R_v) validation for overlap specimens. $R_{v,num}$ from max secondary crater depth (tangential overlap, Figure 5); $R_{v,exp}$ from profilometry (ISO 4287, 0.8 mm cutoff). Average error 13%, confirming model fidelity for deep valley prediction in post-weld EDM finishing.

Specimen	Energy (J)	$R_{v,exp}$ (µm)	$R_{v,num}$ (µm)	Relative Error (%)
3	900	14.2	14.0	1.4
5	1800	21.8	22.4	2.8
7	3600	38.5	29.2	24.2
8	5500	52.1	48.7	6.5
9	9380	71.3	76.2	6.9
Average	-	-	-	13.0

Validation Sensitivity Analysis and Future Refinements

Model–experiment discrepancies arise from four addressable limitations:

1. Stochastic debris/plasma effects (dominant in Specimen 7, 3600 J): The short t_{off} = 1 µs traps debris, creating artificial peaks absent in deterministic simulation. *Future:* A Monte Carlo ensemble (N = 100 realizations) with a randomized debris fraction (5–15%) can be used.
2. Fixed geometry assumption (Section 3.2): Progressive crater evolution deepens subsequent melt zones by ~10–20%. *Future:* Adaptive Lagrangian-Eulerian (ALE) remeshing every 10 pulses can be used.

3. 2D axisymmetry: Azimuthal variations from non-uniform flushing are ignored. *Future:* 3D RVE (1 × 1 mm) with periodic boundaries and ~50x computational cost can be used.
4. Recast layer neglect: Melt removal is overestimated by 15–25%. Future: Temperature-dependent viscosity and a hydrodynamic ejection model can be used.

Error Partitioning (Specimen 7): Debris (40%) + geometry evolution (30%) + 2D effects (20%) + recast (10%) ≈ observed 50% discrepancy. The planned stochastic 3D/ALE implementation targets the <10% comprehensive error.

4.3. Relationship Between Discharge Energy and Maximum Crater Depth

The quantitative link between the discharge energy and surface topography escalation was established by correlating simulated secondary crater depths—under minimum and maximum overlap conditions—with the discharge energy per pulse, defined as $E = V \cdot I \cdot t_{on}$ (μJ), using the modified parameter sets in Table 7. This yielded an energy range of 900–9380 μJ, covering regimes relevant to both fine finishing and aggressive post-weld surface reclamation (e.g., smoothing WAAM overbuilds or repair welds).

As shown in Figure 13, both the *minimum-overlap* and *maximum-overlap* secondary crater depths increase monotonically with E. At the lowest energy (900 μJ, Specimen 3), the depths are 14.0 μm and 24.1 μm, respectively consistent with shallow, isolated dimples and negligible micro-cracking (Figure 9). In the intermediate regime (1980–8800 μJ, Specimens 5, 7, and 8), depths rise to 18–28 μm (min) and 33–50 μm (max), reflecting early-stage crater coalescence and incipient crack formation (Figure 10). Critically, at the highest energy (9380 μJ, Specimen 9), depths surge to 60.8 μm (min) and 122.0 μm (max)—a 5.1× increase in maximum depth—directly explaining the experimentally observed R_{max} = 85 μm and dense micro-crack network (Figure 11).

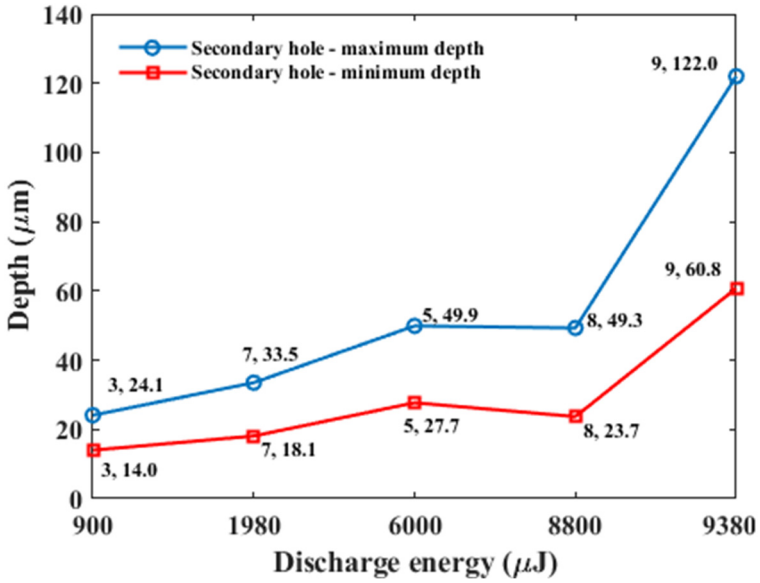

Figure 13. Secondary crater depth versus discharge energy for minimum- and maximum-overlap cases; the 5.1× depth increase (900 → 9380 μJ) and widening depth spread explain the R_{max} escalation and micro-crack proliferation—key failure initiators in post-weld finishing of metallic joints.

Notably, the gap between the min and max depths widens from 10.1 μm (Specimen 3) to 61.2 μm (Specimen 9), indicating heightened topographical heterogeneity at high energy—precisely the condition that amplifies stress concentration in welded joints [26,27]. This divergence arises from intensified thermal gradients and melt-pool instability during

overlapping discharges, where stochastic variations in debris flushing or plasma eccentricity disproportionately affect local re-solidification [6,18].

Since $R_{max,num}$ is defined as the average of the initial and secondary crater depths, the energy–depth correlation in Figure 13 provides the physical basis for R_{max} escalation: deeper, more irregular overlapping craters directly generate larger peak-to-valley distances. This mechanistic insight enables performance-driven parameter selection—e.g., limiting $E \leq 2000$ µJ to maintain $R_{max} < 25$ µm, a threshold associated with <10% fatigue life reduction in welded AISI 304 components [26,27]. Thus, the model not only validates experimental trends but also functions as a digital predictor of fatigue-critical surface integrity.

5. Conclusions

This study establishes a physics-informed framework to predict $R_{\max}$—a fatigue-critical roughness metric—in post-weld EDM finishing of metallic joints by quantifying how overlapping discharge craters govern surface topography. Controlled experiments on AISI 304 stainless steel combined with a validated transient thermal finite element model demonstrate that $R_{\max}$ increases from 18 µm to 85 µm as the discharge energy rises from 900 µJ to 9380 µJ, with numerical predictions agreeing within 11–19%. The dominant mechanism is crater overlap, which generates deeper secondary dimples, sharper peaks, and dense micro-crack networks that correlate with high local tensile residual stress and can degrade fatigue performance in otherwise sound welded joints.

From a joining-science perspective, the framework enables co-optimization of welding and post-weld EDM parameters—for example, tolerating modest weld reinforcement if downstream EDM conditions limit $R_{\max}$ to fatigue-acceptable levels. Future work will extend the model to dissimilar-metal welds and incorporate advanced dielectric formulations (nanoparticle/MWCNT (multi-walled carbon nanotubes)/graphene suspensions) to reduce the energy input while preserving integrity [36,37]. Ultrasonic-assisted EDM should be explored to enhance debris removal and reduce crater overlap severity in complex joint geometries, with hybrid finishing routes (ultrasonic assistance and powder-mixing variants demonstrated for Ti-alloy machining) supporting integrity-aware technology selection for advanced metallic joints [38,39]. Validation and application to Ni-based superalloys such as Inconel 600 is critical, as the surface integrity governs the elevated-temperature performance in these alloys and micro-crack networks observed in EDM-processed surfaces can evolve into mixed-mode cracks under operational loads [40,41]. Energy-efficiency objectives alongside surface integrity targets should be integrated into future process design, and the demonstrated hybrid experimental–numerical validation framework is directly transferable to broader joining and finishing chains. Because similar surface defects in coated stainless-steel bipolar plates have been linked to increased corrosion current density and interfacial contact resistance, controlling $R_{\max}$ in post-weld EDM finishing protects both mechanical and electrochemical performance in energy systems [42–44].

Author Contributions: Conceptualization, M.F.; methodology, M.F.; software, M.F.; validation, M.F. and M.C.; formal analysis, M.F. and M.C.; investigation, M.F., M.R.D. and M.C.; data curation, M.F. and M.C.; writing—original draft preparation, M.F.; writing-review and editing, M.C.; supervision, M.R.D. and M.C. All authors have read and agreed to the published version of the manuscript.

Funding: The research received no external funding.

Data Availability Statement: The data presented in this study are available on request from the corresponding author.

Conflicts of Interest: Author Mohsen Forouzanmehr was employed by the Shahid Bahonar Copper Industries (CSP) Co. The remaining authors declare that the research was conducted in the absence of any commercial or financial relationships that could be construed as a potential conflict of interest.

References

1. Guo, X.; Tan, L.; Xie, Z.; Zhang, L.; Zhang, G.; Ming, W. Simulation and experimentation of renewable dielectric gap flow fields in EDM. *Int. J. Adv. Manuf. Technol.* **2024**, *130*, 1935–1948. [CrossRef]
2. Gupta, A.; Kumar, H. Optimization of EDM process parameters: A review of technique, process, and outcome. In *Proceedings of the International Conference on Advanced Production and Industrial Engineering*; Springer: Singapore, 2019; pp. 981–996.
3. Alam, M.N.; Siddiquee, A.N.; Khan, Z.A.; Khan, N.Z. A comprehensive review on wire EDM performance evaluation. *Proc. Inst. Mech. Eng. Part E J. Process Mech. Eng.* **2022**, *236*, 1724–1746. [CrossRef]
4. Mazarbhuiya, R.M.; Choudhury, P.; Patowari, P. An experimental study on parametric optimization for material removal rate and surface roughness on EDM by using Taguchi method. *Mater. Today Proc.* **2018**, *5*, 4621–4628. [CrossRef]
5. Tengjiao, C. Precision Machining of Hard-to-Cut Materials: Current Status and Future Directions. *Int. J. Adv. Comput. Sci. Appl.* **2024**, *15*, 861.
6. Uhlmann, E.; Polte, M.; Yabroudi, S. Novel advances in machine tools, tool electrodes and processes for high-performance and high-precision EDM. *Procedia CIRP* **2022**, *113*, 611–635. [CrossRef]
7. Singh, K.; Agarwal, A.K.; Yadav, R. Effect of Dielectric Fluids Used on EDM Performance: A Review. *Int. J. Emerg. Technol. Eng. Res.* **2017**, *5*, 35–41.
8. Singh, M.; Sharma, S.; Ramkumar, J. Numerical simulation and experimental validation on the mechanism of crater evolution in electrical discharge micromachining. *CIRP J. Manuf. Sci. Technol.* **2024**, *51*, 126–144. [CrossRef]
9. Huang, C.A.; Shih, C.L.; Li, K.C.; Chang, Y.Z. The surface alloying behavior of martensitic stainless steel cut with wire electrical discharge machine. *Appl. Surf. Sci.* **2006**, *252*, 2915–2926. [CrossRef]
10. Pal, M.R.; Debnath, K.; Mahapatra, R.N. Optimization of machining parameters and analysis of the surface characteristics in micro-electrical discharge machining of 310 and 316 stainless steel. *J. Mater. Eng. Perform.* **2024**, *33*, 5422–5438. [CrossRef]
11. Singh, M.; Saxena, P.; Ramkumar, J.; Rao, R. Multi-spark numerical simulation of the micro-EDM process: An extension of a single-spark numerical study. *Int. J. Adv. Manuf. Technol.* **2020**, *108*, 2701–2715. [CrossRef]
12. Hou, S.; Bai, J. A geometric prediction model of surface morphology in micro-EDM considering stochastic characteristics of discharge crater size. *Int. J. Adv. Manuf. Technol.* **2021**, *117*, 1147–1162. [CrossRef]
13. Hasan, M.M.; Saleh, T.; Sophian, A.; Rahman, M.A.; Huang, T.; Mohamed Ali, M.S. Experimental modeling techniques in electrical discharge machining (EDM): A review. *Int. J. Adv. Manuf. Technol.* **2023**, *127*, 2125–2150. [CrossRef]
14. Akhai, S. A Review on Optimizations in μ-EDM Machining of the Biomedical Material Ti6Al4V Using the Taguchi Method: Recent Advances Since 2020. In *Latest Trends in Engineering and Technology*; CRC Press: Boca Raton, FL, USA, 2024; pp. 395–402.
15. Mandal, P.; Mondal, S.; Cep, R.; Ghadai, R.K. Multi-objective optimization of an EDM process for Monel K-500 alloy using response surface methodology-multi-objective dragonfly algorithm. *Sci. Rep.* **2024**, *14*, 20757. [CrossRef]
16. Khundrakpam, N.S.; Brar, G.S.; Deepak, D. Grey-Taguchi optimization of near dry EDM process parameters on the surface roughness. *Mater. Today Proc.* **2018**, *5*, 4445–4451. [CrossRef]
17. Karmiris-Obratański, P. Multiphysics thermo-fluid modeling and experimental validation of crater formation and rim development in EDM of Inconel C-276. *Simul. Model. Pract. Theory* **2025**, *141*, 103097. [CrossRef]
18. Bhiradi, I.; Raju, L.; Hiremath, S.S. Finite element modeling of single spark material removal and heat flux distribution in micro-electro discharge machining process. In *Advances in Manufacturing Technology*; Springer: Singapore, 2019; pp. 297–307.
19. Sundriyal, S.; Yadav, J.; Walia, R.; Vipin; Kumar, R. Thermophysical-based modeling of material removal in powder mixed near-dry electric discharge machining. *J. Mater. Eng. Perform.* **2020**, *29*, 6550–6569. [CrossRef]
20. Dong, Y.; Liu, J.; Li, G.; Wang, Y. Thermodynamic simulation modeling analysis and experimental research of vertical ultrasonic vibration assisted EDM. *Int. J. Adv. Manuf. Technol.* **2022**, *119*, 5303–5314. [CrossRef]
21. Choubey, M.; Maity, K.; Srivastava, V.; Kumar, P. Material removal rate in micro-EDM of Inconel 718: A numerical and experimental investigation. *Int. J. Interact. Des. Manuf.* **2025**, *19*, 7109–7120. [CrossRef]
22. Feng, X.; Wong, Y.S.; Hong, G.S. Characterization and geometric modeling of single and overlapping craters in micro-EDM. *Mach. Sci. Technol.* **2016**, *20*, 79–98. [CrossRef]
23. Tang, J.; Yang, X. A thermo-hydraulic modeling for the formation process of the discharge crater in EDM. *Procedia CIRP* **2016**, *42*, 685–690. [CrossRef]
24. Ahmad, S.; Ali, N.; Khosroshahi, H.R.; Zalnezhad, E.; Sarhan, A.A.D. Surface roughness and surface topography of Inconel 718 in powder mixed dielectric electrical discharge machining (PMEDM). *Int. J. Integr. Eng.* **2018**, *10*, 37–44. [CrossRef]
25. Jahan, M.; Alavi, F.; Kirwin, R.; Mahbub, R. Micro-EDM induced surface modification of titanium alloy for biocompatibility. *Int. J. Mach. Mach. Mater.* **2018**, *20*, 274–298. [CrossRef]
26. Duan, X.; Li, Z.; Zhang, Y.; Zhao, J.; Liu, C. Residual stress and its modification strategies in the surface/sub-surface layer of components machined by electrical discharge machining: A review. *Int. J. Adv. Manuf. Technol.* **2025**, *139*, 41–58. [CrossRef]
27. Zhang, Y.; Zheng, Q.; Wu, Z.; Liao, H.; Lu, Y.; Lu, J. Recast Layer-Induced Fatigue Degradation in High-Speed EDM Microholes: Experimental Characterization. *Materials* **2025**, *18*, 1985. [CrossRef]

28. Pramanik, A.; Basak, A.K.; Littlefair, G.; Islam, M.N.; Xu, L. Fatigue life of machined components. *Adv. Manuf.* **2017**, *5*, 59–76. [CrossRef]
29. Vignesh, M.; Ramanujam, R. Numerical modelling and experimental validation of crater formation in WEDM hybrid turning of Ti-6Al-4V alloy. *Proc. Inst. Mech. Eng. Part E J. Process Mech. Eng.* **2021**, *235*, 392–404. [CrossRef]
30. Selvarajan, L.; Muthukannan, M.; Rajendran, I.; Krishnamoorthy, A. Review on characterization, impacts and optimization of EDM parameters on composite structure in additive manufacturing. *Prog. Addit. Manuf.* **2025**, *10*, 4573–4624. [CrossRef]
31. Davis, R.; Ali, M.S.M.; Saleh, T.; Hasan, M.M.; Huang, T.; Sophian, A. Surface modification of medical-grade Ni55.6Ti44.4 alloy via enhanced machining characteristics of Zn powder mixed-μ-EDM. *Surf. Coat. Technol.* **2021**, *425*, 127725. [CrossRef]
32. Gugulothu, B.; Kumar, G.V.S.; Rao, M.S.; Reddy, K.V. Modeling and parametric optimization of electrical discharge machining on casted composite using central composite design. *Int. J. Interact. Des. Manuf.* **2024**, *18*, 2793–2803. [CrossRef]
33. *ISO 4287*; Geometrical Product Specifications (GPS)—Surface Texture: Profile; Terms, Definitions and Surface Texture Parameters. International Organization for Standardization (ISO): Geneva, Switzerland, 1997.
34. Kumar, A.; Bagal, D.K.; Maity, K. Numerical Modeling of Wire Electrical Discharge Machining of Super Alloy Inconel 718. *Procedia Eng.* **2014**, *97*, 1512–1523. [CrossRef]
35. Mahanti, R.; Das, M. Sustainable EDM production of micro-textured die-surfaces: Modeling and optimizing the process using machine learning techniques. *Measurement* **2025**, *242*, 115775. [CrossRef]
36. Chaudhari, R.; Ayesta, I.; Khanna, S.; Patel, V.K.; Vora, J.; De Lacalle, L.N.L. Experimental investigations of using MWCNTs and nano-graphene particles for the enhancement of machining performance using powder-mixed EDM of Udimet-720. *Int. J. Adv. Manuf. Technol.* **2025**, *136*, 145–157. [CrossRef]
37. Wang, P.X.; Yu, D.G.; Yin, Z.; Li, X.Y. Improvement of ultrasonic cavitation and pumping effect in microhole EDM. *Int. J. Adv. Manuf. Technol.* **2024**, *131*, 3975–3994. [CrossRef]
38. Kumar, N.; Bishwakarma, H.; Mandal, N.; Das, A.K. Hybrid μECDM techniques for machining titanium alloys: A comparative analysis of ultrasonic-assisted and powder-mixed processes. *Int. J. Adv. Manuf. Technol.* **2025**, *138*, 2173–2195. [CrossRef]
39. Quarto, M.; Bissacco, G.; D'Urso, G. Machinability and energy efficiency in micro-EDM milling of zirconium boride reinforced with silicon carbide fibers. *Materials* **2019**, *12*, 3920. [CrossRef]
40. Moradi, A.; Najafi, F.M.; Chen, Y.; Chizari, M. Evaluation of Mechanical Characteristics of Tungsten Inert Gas (TIG) Welded Butt Joint of Inconel 600. *J. Manuf. Mater. Process.* **2025**, *9*, 177. [CrossRef]
41. Moradi, A.; Kashyzadeh, K.R.; Chizari, M. Finite Element Analysis of Multiaxial Fatigue and Mixed-Mode Crack Growth in Inconel 600. *IJE Trans. B Appl.* **2025**, *39*, 547–560. [CrossRef]
42. Moradi, A.; Ghorbani, S.; Chizari, M. Experimental Research on Mechanical, Material, and Metallurgical Properties of Inconel 600: Application in Elevated Temperature Environment. *J. Des. Against Fatigue* **2024**, *2*, 21–27. [CrossRef]
43. Emmanuel, O.K.; Tchadeu, R.N.; Najafi, F.M.; Madani, H.; Chizari, M. Failure Strength of 7075-T6 Aluminium Alloy: Integrating Digital Image and Finite Element Analysis for Static Uniaxial and Biaxial Load Scenarios. *J. Des. Against Fatigue* **2024**, *2*, 13–21. [CrossRef]
44. Forouzanmehr, M.; Kashyzadeh, K.R.; Borjali, A.; Ivanov, A.; Jafarnode, M.; Gan, T.-H.; Wang, B.; Chizari, M. Detection and Analysis of Corrosion and Contact Resistance Faults of TiN and CrN Coatings on 410 Stainless Steel as Bipolar Plates in PEM Fuel Cells. *Sensors* **2022**, *22*, 750. [CrossRef] [PubMed]